Wideband luminescence from bandgap-matched Mg-based Si core-shell geometry nanocomposite

Cite as: AIP Advances **8**, 055324 (2018); https://doi.org/10.1063/1.5019167
Submitted: 11 December 2017 . Accepted: 19 April 2018 . Published Online: 23 May 2018

Adem Kocyigit, Noha Elhalawany, Ersin Bahceci, Brian Enders, Krithik Puthalath, Laila Abuhassan, Zain Yamani, and Munir Nayfeh

Wideband luminescence from bandgap-matched Mg-based Si core-shell geometry nanocomposite

Adem Kocyigit,[1] Noha Elhalawany,[2] Ersin Bahceci,[3] Brian Enders,[4] Krithik Puthalath,[4] Laila Abuhassan,[5] Zain Yamani,[6] and Munir Nayfeh[4,a]
[1]*Department of Electrical and Electronic Engineering, Igdir University, Igdir, Turkey*
[2]*Polymers and Pigments Department, National Research Center, Cairo, Egypt*
[3]*Department of Metallurgical and Materials Engineering, Iskenderun Technical University, Hatay, Turkey*
[4]*Department of Physics, University of Illinois at Urbana-Champaign, 1110 W. Green Street, Urbana, Illinois 61801, USA*
[5]*Department of Physics, University of Jordan, Amman 11941, Jordan*
[6]*Department of Physics, King Fahd University, Dhahran 34463, Saudi Arabia*

(Received 11 December 2017; accepted 19 April 2018; published online 23 May 2018)

We use wet treatment to integrate red-luminescent Si nanoparticles with Mg-based wide-bandgap insulators Mg(OH) and MgO (5.7 and 7.3 eV respectively). In the process, Mg^{2+} is reduced on Si nanoparticle clusters, while suffering combustion in water, producing a spatially inhomogeneous $Mg(OH)_2$/MgO-Si nanoparticle composite with an inner material predominantly made of Si, and a coating consisting predominantly of magnesium and oxygen ("core-shell" geometry). The nanocomposite exhibit luminescence covering nearly entire visible range. Results are consistent with formation of $Mg(OH)_2$/MgO phase with direct 3.43-eV bandgap matching that of Si, with in-gap blue-green emitting states of charged Mg and O vacancies. Bandgap match with nanocomposite architecture affords strong enough coupling for the materials to nearly act as a single hybrid material with novel luminescence for photonic and photovoltaic applications. https://doi.org/10.1063/1.5019167

I. INTRODUCTION

Magnesium[1–3] and its compounds, such as wide-band gap insulators magnesium oxide and magnesium hydroxide (7.8 and 5.7 eV respectively) have received wide scientific interest in the last decade as they have applications in catalysis,[4] toxic waste remediation,[5] additives in refractory, paint, superconductor products,[6–8] and in steel manufacturing because of its high corrosion-resistant behavior.[9] Nanostructures of MgO and $Mg(OH)_2$ have recently received much attention due to potential magnetic and optical novel properties stemming from Mg or O vacancies. Whereas bulk MgO is a diamagnetic material,[10] nanocrystalline MgO powders display a ferromagnetic state,[11,12] attributed to Mg vacancy defects near the surface of nanograins with magnetic moments being dependent on the size of nanoparticles via dependence on the concentration of Mg vacancies. Also, unpaired electrons trapped at oxygen vacancy sites, as was found in highly defective MgO nanosheets, may produce magnetic features.[13] Furthermore, density functional calculations have suggested that C or N can be substituted for oxygen in MgO, which form impurity pairs that may interact antiferromagnetically with p-type MgO.[14] The nanomaterials exhibit several interesting optical features stemming from intrinsic Mg and O vacancies or from extrinsic doping. MgO nanograins may act as host for luminescent transition and rare earth doping affording a wide range of applications including phosphors, solid electrolytes, and chemical sensors.[15] For example, doping with

[a]Corresponding author: m-nayfeh@illinois.edu

Fe^{3+} affords energy transitions covering both high and low energy regions, with broad tunable emission/absorption bands.[16,17] Incomplete conversion of $Mg(OH)_2$ nanostructures to MgO create vacancies, which can be used to engineer intermediate nanomaterial with distinct optical bandgap (3.43 eV for example), which affords the nanostructures novel emission bands in the UV and visible regions.[18]

$Mg(OH)_2$ nanostructures are synthesized by several methods, such as electrodeposition,[19] sol–gel technique,[20] precipitation,[21] hydrothermal,[22] solvothermal[23] and microwave assisted synthesis.[24] The synthesis of MgO nanostructures, on the other hand, may be carried out from $Mg(OH)_2$ by simple thermal treatment (at 350 °C) which releases water molecules. Another procedure that removes water and hence convert $Mg(OH)_2$ to MgO is calcination at 450 °C.[25,26]

The existence of an intermediate $Mg(OH)_2$/MgO phase with an optical bandgap that can be engineered gives the opportunity to incorporate its attributes into silicon by creating a nanocomposite that strongly couples the two materials electronically and optically. In this paper, we use wet treatments to integrate silicon-based material with Mg-based material in nanocomposite structures. In the process Mg^{2+} is reduced on clusters of red-luminescent 2.9±0.1 nm Si nanoparticle (2.2 eV and 3.4 eV confinement and direct bandgaps respectively), while suffering combustion with water, producing $Mg(OH)_2$/MgO-Si nanoparticle composite. The nanocomposite exhibit luminescence covering the entire visible: red, green and blue (RGB). Those optical features are consistent with formation of an intermediate $Mg(OH)_2$/MgO phase of a low direct bandgap (3.43 eV) with enhanced formation of charged states of Mg and O vacancies that allow strong electronic coupling and integration with the 3.4-eV direct bandgap Si-based material, making the two material act nearly as a single hybrid material. The coupling is enhanced not only by electronic/optical gap matching but also geometrically by the composite architecture that reduces inter material spacing. Composite architecture affords novel luminescence for photonic and photovoltaic applications.

II. EXPERIMENTAL

We used ultra-small Si nanoparticles[27–31] with Si-H termination. The nanoparticles are prepared from Si wafers by chemical etching in HF and H_2O_2 using electrical or hexachloroplatinic acid catalyst. The nanoparticles are recovered from the treated wafer using an ultrasound treatment into a solvent of choice, such as isopropyl alcohol using ultrasound. The dispersed nanoparticles may subsequently be delivered from the liquid on a target using several delivery procedures, including electrospray, atomization, spin coating, or drop-drying. TEM image of a typical nanoparticle sample deposited on a graphite grid gives a histogram with counts of 4, 56, 12, 9, and 2 at diameters of 3.5, 2.9, 2.2, 1.7, and 1 nm, respectively, giving an average diameter of 2.65±0.5 nm, with a predominant diameter of 2.9-nm. This is more of a normal than log-normal distribution.

For magnesium ions Mg^{2+}, we dissolve in water Mg salt such as a chloride, sulfate or nitrate. In the procedure, 0.5 ml of 1.65×10^{-3} M $MgCl_2$ water solution is added to 10 ml of Si nanoparticles in IPA (10 μM).

The materials and structures are characterized using several procedures including scanning electron microscopy (SEM), X-ray photoelectron spectroscopy, and imaging and material analysis mapping using Energy-dispersive X-ray spectroscopy (EDS), while the optical properties are characterized using photoluminescence spectroscopy, fluorescence microscopy, and Fourier transform infrared spectroscopy (FTIR). To obtain the luminescence spectra, we excite particles by 365-, 300- or 254-nm incoherent light. For detection, we use a fiberoptic spectrometer. It uses optical fibers to extract the emission. We use a holographic grating. It is a near-infrared grating with groove density of 600/mm with a blaze wavelength of 0.4 μm and with best efficiency in the range 0.25–0.80 μm.

III. RESULTS

Since the nanoparticles exhibit a luminescent band (550-700 nm emission band), we monitored changes in the nanoparticle formation by monitoring the photoluminescence using UV light excitation. We monitored the reaction solution aperiodically while being irradiated with UV radiation from

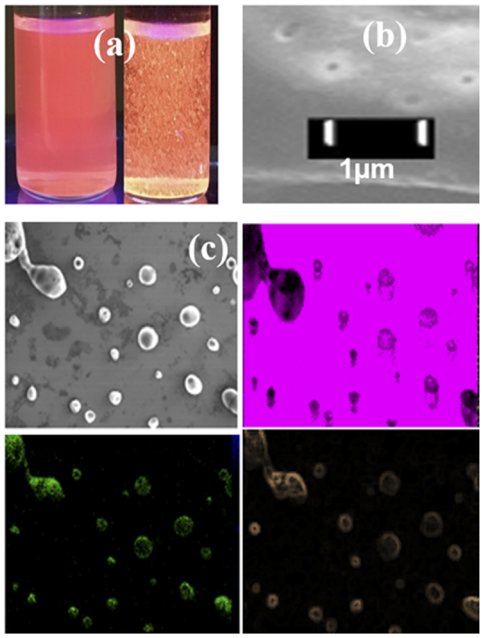

FIG. 1. (a) Luminescent photos of colloids after interaction of silicon nanoparticles with Mg^{2+} ions (right) Si nanoparticles in isopropanol alcohol and Mg^{2+} in water after seven hours of mixing the components. It clearly shows clustering and precipitation and a change in color observed by naked eye from the red towards the yellow (left) control solution in the absence of water where the magnesium salt is dissolved in IPA instead of water. All vials are 15 mm in diameter. (b) Scanning electron microscope (SEM) images of a thin film made on a silicon wafer by drying a drop from the colloid, showing isolated nanocomposite structures. The structures consist of a dark core surrounded by a lighter layer. (c) Material analysis (four frames) using energy-dispersive X-ray spectroscopy (EDX). The inner region is associated with Si, while the outer region is associated with magnesium and oxygen. The color code is: total composition (black and white), silicon (pink), magnesium (orange) and oxygen (green). The nanocomposite points to a spatially inhomogeneous architecture with a denser inner material predominantly made of Si, and a lighter outer layer consisting predominantly of magnesium and oxygen.

a mercury lamp with a wavelength of 365 nm. In control mixtures as shown in Figure 1a (left) prepared in the absence of water, i.e. both the magnesium salt and the Si nanoparticles are dissolved in IPA, measurements show no clustering or change in luminescence color. Figure 1a (right) gives a luminescent photo of the solution of Si nanoparticles in isopropanol alcohol and Mg^{2+} in water after seven hours of mixing the components. It clearly shows clustering and precipitation and a change in color observed by naked eye from the red towards the yellow. Moreover, Figure 1a (right)) shows no significant luminescence loss (quenching).

A very thin film of the colloid was prepared by dispensing one drop of the suspension on a device quality Si wafer placed on a hot plate kept at 40 °C. Figure 1b presents SEM images of isolated core-shell structures. They are large enough to be easily observed by SEM. They consist of a dark inner component surrounded by a lighter lower density component. Energy-dispersive X-ray spectroscopy (EDX) provided elemental analysis and material mapping. Figure 1c (four frames) shows that the denser inner material is predominantly made of Si, while the lighter coating consists predominantly of magnesium and oxygen.

The X-ray photoelectron spectrum given in Figure 2 shows a wide peak having a binding energy of 51.66 eV, close to that of Mg silicates, which is known to occur at 51.6 eV,[32] indicating the existence of Mg-based-Si nanostructure. The wide XPS band when analyzed shows it consists of two additional smaller bands at 49.5 and 50.8 eV, which correspond to Mg (2p) core level for Mg, and MgO, respectively,[32] indicating a nanocomposite with an outer layer which contains magnesium, oxygen, and silicon (silicate). Because the film is a random distribution of the nanocomposite particles, with an inhomogeneous thickness, while the silicon component is a random cluster of ultra small H-terminated silicon nanoparticles while the coating is expected to be an amorphous layer of the oxides, XRD measurements did not show any crystallinity structure.

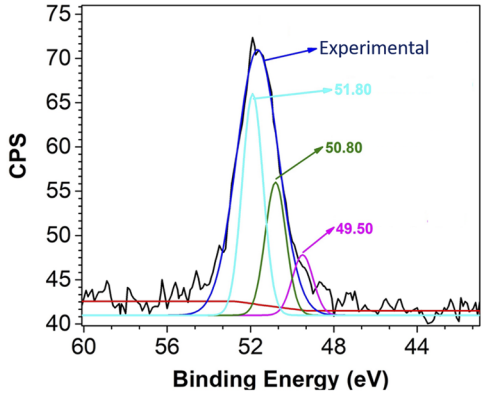

FIG. 2. X-ray photoelectron spectrum showing a wide peak having a binding energy of ~ 51.66 eV. Analysis gives three components: at 49.5, 50.8, and 51.8 eV typically known for Mg, MgO, and MgSi in silicate respectively. The blue curve is a re-digitized curve of the experimental data.

The nanocomposite formation points to a mechanism as shown in the schematic in Figure 3. The nanoparticles form stable dispersions in isopropyl alcohol (IPA), but being hydrophobic they form clusters in water, with diameters in the range 100-500 nm. When Si nanoparticles in isopropanol are mixed with magnesium salt in water, nanoparticle clusters form. Mg^{2+} and clusters of nanoparticles are attracted to each other by polarization forces, followed by exchange of holes from Mg^{2+}, which oxidize silicon.[33] The reduced Mg simultaneously suffers combustion with water to produce $Mg(OH)_2$ and hydrogen: $Mg(s) + 2H_2O(g) \rightarrow Mg(OH)_2(aq) + H_2(g)$. Unlike bulk, Mg in powder or sub-micron form reacts vigorously with water exothermally.[34] $Mg(OH)_2$ is a low-solubility mineral brucite which could form solid precipitate coating on Si grains. As the photoluminescence showed stability, Si is not consumed while the shell may have provided protective cladding against luminescence quenching by water. Bare Si is able to reduce Mg^{2+} to metal[33,35] because the electro negativity of Mg is lower than

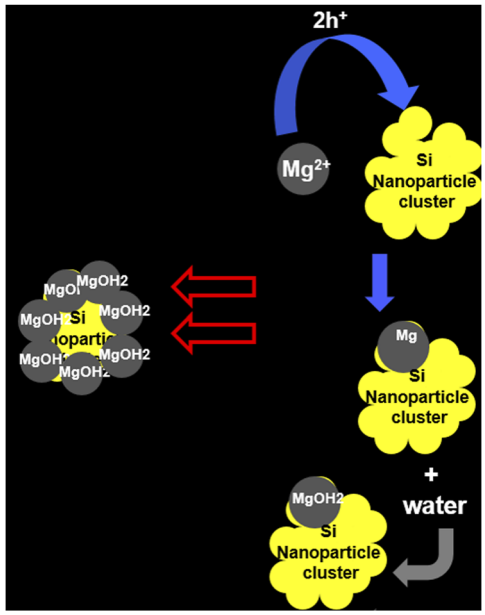

FIG. 3. Cartoon of the formation of the nanocomposite structures. Mg^{2+} and clusters of nanoparticles that form (due to the hydrophobicity of silicon nanoparticles in water) are attracted to each other by polarization forces, followed by exchange of holes from Mg^{2+} to oxidize silicon, while the reduced Mg simultaneously suffering combustion with water to produce $Mg(OH)_2$ and hydrogen gas.

that of bare Si, i.e., lower reduction potential (-2.37 V compared to -0.85 V), which favors exchange of holes.[36] In the presence of surface hydrogen on silicon, the silicon's standard reduction potential becomes ~ - 0.45 V, making hole exchange more efficient. Moreover, spatial quantum confinement and strong surface re-construction in nano Si, considerably reduce electron affinity and make Si-H bonds become highly polarizable.

We analyzed the molecular vibrations of the structures using Fourier transform infrared spectroscopy (FTIR). Samples were prepared on Si as well as glass substrates. Figure 4a displays the FTIR spectra of the as prepared nanocomposite in the energy range 2500-4000 cm^{-1}. The broad bands at high frequencies extending from 3400 to 3200 cm^{-1} are due to the symmetric and asymmetric stretching modes of the hydroxyl group. The peak intensity of the free hydroxyl group (Mg–OH) stretching mode at 3700 cm^{-1} appears as a slightly shifted kink at 3633 cm^{-1}. The appearance of Mg-based system as a kink has been known in the literature.[37,38] An exercise of differentiation of the experimental curve gives a dispersion-like peak near the kink as shown in Figure 4b. This can be demonstrated using the work of Dhaouadi et al[39] shown in Figure 5a (adapted from Ref. 39). In wet samples, the signature of Mg(OH)2 appears as a significant sharp peak. But under thermal drying to MgO, as shown in Figure 5a, the peak becomes smaller and smaller with temperature, transforming into a kink when the temperature reaches 400 °C. (A vertical line was drawn through the feature is used to guide the eye). We simulated the kink feature with a sum of two Gaussians, one wide and the other sharp (Figure 5b top). The bound (-OH) component was approximated by a Gaussian with broad width while the free (Mg-OH) component by narrower Gaussians; and the relative positions, heights and widths are optimized. It shows reasonable display of the feature and agreement with the experimental spectrum near 3600-3700 cm^{-1} as shown in Figure 5b bottom. Differentiation of the theoretical sum of the two Gaussians near the kink feature, would give a smooth line due to the wide Gaussian while the sharp Gaussian would give a dispersion-like peak. Thus the presence of a kink in this range points to a small but indeed non-zero presence of Mg-based species. It should be noted that there are other molecular bonds that may be associated with other features in the FTIR. The bending modes of the adsorbed water molecules appear as a weak band around 1680 cm^{-1}. The two residual bands observed in the IR spectra at 2922and 2850 cm^{-1} can are attributed to the stretching mode of $-CH_2$ and $-CH_3$ groups of residual organic surfactant, possibly from residual IPA; their bending

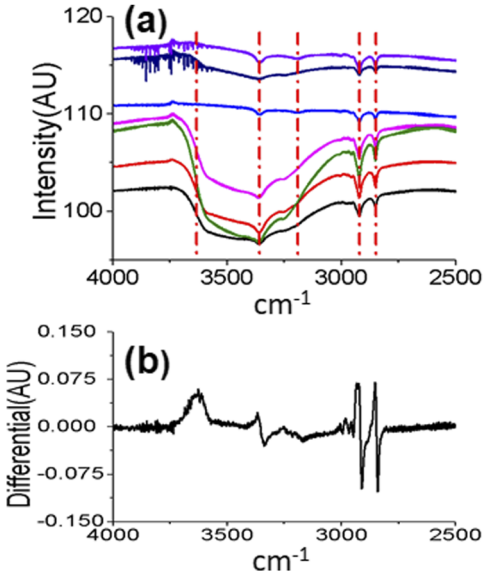

FIG. 4. Molecular composition using Fourier transfer infrared spectroscopy (FTIR) in the range 2500-4000 cm^{-1}. (a) FTIR spectra of the Si-$Mg(OH)_2$/Si-MgO samples prepared on substrates. The broad bands at high frequencies in the 3400 to 3200 cm^{-1} range are due to the symmetric and asymmetric stretching modes of the hydroxyl groups bound or free. The peak intensity of the free hydroxyl group (Mg–OH) stretching mode, which appears usually as a sharp peak at 3700 cm^{-1} is very small. (b) Differential of the spectrum in (a) revealing the presence of peak at ~ 3700 cm^{-1}.

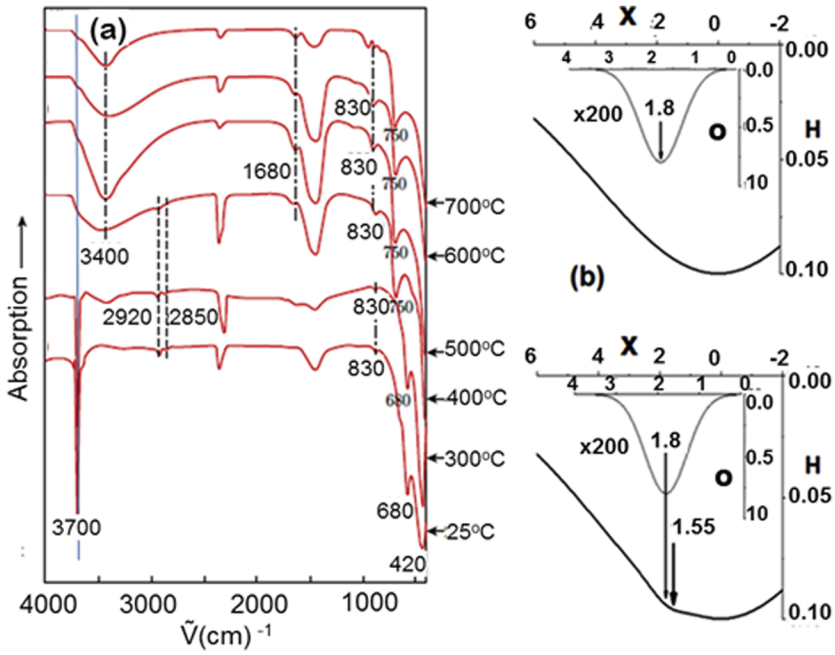

FIG. 5. (a) Several FTIR spectra recorded during thermal drying of $Mg(OH)_2$ to MgO, showing that the Mg-based structure at ~3700 cm^{-1} becoming smaller and smaller then turning into a kink (Reproduced with permission from H. Dhaouadi and F. Touati, Nano-Micro Lett. **3**, 153–159 (2011). Copyright 2011 Springer Publishing.) (b) Simulation of kink features with a sum of two Gaussians. It displays the non-dimensional height H as a function of the non-dimensional frequency x of two Gaussians, one with broad width and the other with a narrow width. (top) plots of the narrow and wide Gaussians individually (bottom) plots of the narrow and the sum of the narrow and wide Gaussians displaying the kink feature.

modes $-CH_2$ and $-CH_3$ are expected in the range 1700–1400 cm^{-1}.[40] The signature of Si in the FTIR spectrum falls in the low energy region. Figure 6 gives an FTIR response in the range 600-4000 cm^{-1} of films prepared on a silicon substrate instead of a glass substrate to allow transmission measurements in the low energy regime as glass does not have good transmission in this region. First we observe a transmission peak at ~ 1030 cm^{-1}, which can plausibly be associated with Si-O-Mg. The absorption band of asymmetric stretching vibrations of Si–O lies typically at 1090 cm^{-1}. However it has been noted in the literature that in the presence of Mg the band shift to 1040–1024 cm^{-1}; and that the change of vibration frequency may plausibly be connected with asymmetric vibrations of Si–O bond in Si–O–Mg bridge groups.[41] Secondly we observe additional Mg-based response at 670 cm^{-1}, which may point to another vibration mode of Si–O–Mg.[41]

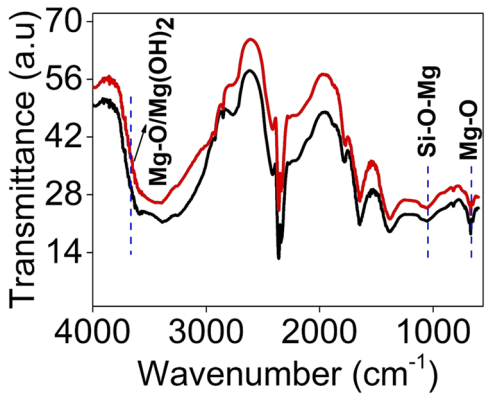

FIG. 6. Molecular composition using Fourier transform infrared spectroscopy (FTIR) of Si-$Mg(OH)_2$ samples prepared on silicon substrates in the range 600-4000 cm^{-1}.

We studied the photoluminescence from a thin film, which was formed by drop drying of a certain volume of the reaction solution on a glass substrate kept at a temperature of 40 °C. Luminescent images were taken under UV excitation. Figure 7a is luminescent photo of the film taken with excitation at 365 nm. The blue/purple color is caused by scattering of incident ultraviolet (UV); it shows that the film is not homogeneous. We recorded the photoluminescence spectra from small spots (1-2 mm across) using a fiber optic sensor with UV excitation at a wavelength of 365 nm as shown in Figure 7b. It shows a wide spectrum extending over the range 400-700 nm with a band maximum at 574 nm. We also observe a local blue-green photoluminescence band (500-525 nm) peaking at 515 nm.

The 550-740 nm red luminescence band of isolated Si nanoparticles is also shown in Figure 7b. The two spectra give a peak shift from 626 nm (1.98 eV) to 574 nm (2.134 eV), corresponding to a shift of 0.15 eV. It is to be noted that MgO (or $Mg(OH)_{2)}$ is known to exhibit a weak broad luminescent band in the UV-blue range of the spectrum as shown in Figure 8a–b. Figure 8a gives the photoluminescence under 290 nm wavelength excitation, showing hints of sub peaks. Detailed fitting by the authors gave sub bands at 362, 387, 410, 434 nm.[42] Figure 8b gives the photoluminescence using excitation at a wavelength of 385 nm. The spectrum clearly shows sub peaks at 432, 465, and 495nm.[43] Note that luminescence given in Figure 8 is excitation wavelength-dependent. Figure 8b is generated by excitation at 395 nm, whereas 8a is generated by excitation at 290 nm. The sub luminescent peaks were attributed to emission from in-gap emitting states, resulting from charged Mg and O vacancies. By integrating the area under the normalized spectra in Figure 7b (previously Figure 6b) shows that the blue-green is ~ 37 percent of the total emission of the nanocomposite, compared to blue-green of only 7 percent of the total emission in isolated Si nanoparticles.

We believe the emergence of the three features: strong blue-green luminescence, which is normally weak in isolated Mg-based systems; the band (500-525 nm) peaking at 515 nm in the spectrum; as well as the strong shift are related to the effect of coupling of magnesium-based system ($MgO/Mg(OH)_2$/Mg/Mg silicates) to the silicon system. In fact, the appearance of the 500-525 nm band with a peak at 515 nm in the overall spectrum shows the finger print of the Mg-based being

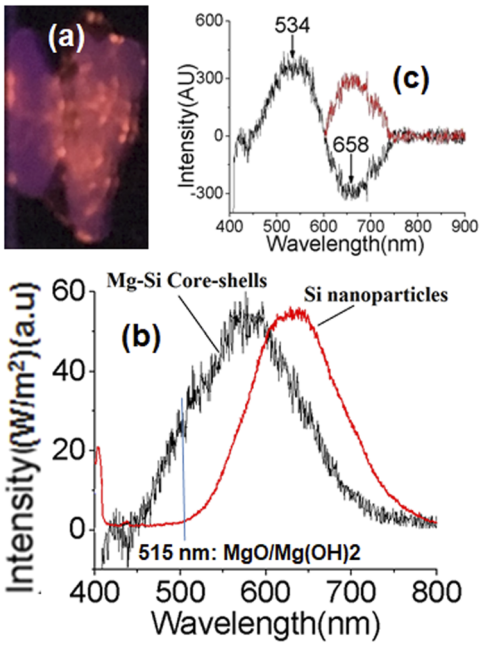

FIG. 7. Photoluminescence of a thin film on a glass substrate formed by drop drying at a temperature of 40 °C. (a) Luminescent image taken under UV excitation under 365 nm excitation. The blue/purple color is caused by scattering of incident ultraviolet (UV). (b) Normalized photoluminescence spectra for the nanocomposite structures, and isolated silicon nanoparticle colloid, taken using UV excitation at a wavelength of 365 nm. (c) Difference between the normalized nanocomposite and the isolated nanoparticles spectra. The negative difference has been inverted to a positive spectrum for display.

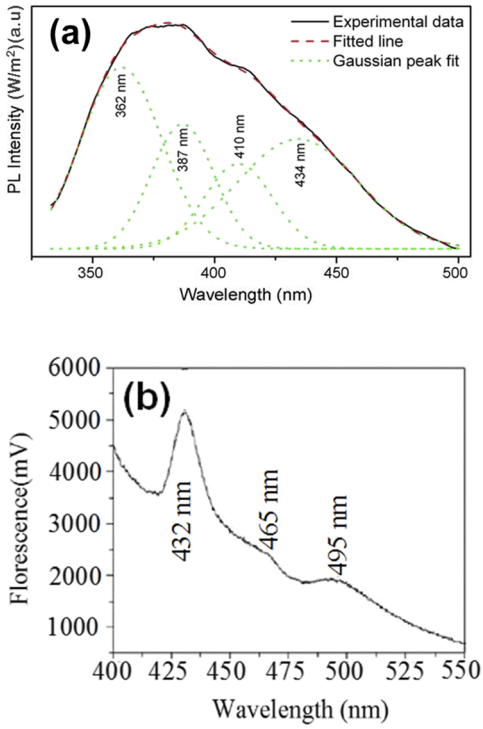

FIG. 8. Photoluminescence from $Mg(OH)_2/MgO$ (a) using 290 nm wavelength excitation, showing hints of sub peaks at 362, 387, 410, 434 nm. (Reproduced with permission from Kumari *et al.*, Ceramics International **35**, 3355–3364 (2009). Copyright 2009 Elsevier Publishing.) (b) using 385 nm wavelength excitation, clearly showing sub peaks at 432, 465, and 495nm. (Reproduced with permission from Balamurugan *et al.*, J. Nanotechnol. **2014**, 1. Copyright 2014 Hindawi Publishing Corporation.)

imprinted on the core shell photoluminescence, which may indicate strong energy transfer. For illustration of the blue band, Figure 7c gives the difference between the normalized core-shell and the isolated nanoparticles spectra. The negative difference has been inverted to a positive spectrum for display.

IV. ANALYSIS AND DISCUSSION

The luminescence and the proposed energy transfer may now be discussed with the aid of the schematic of the partial energy level diagram of Si nanoparticles, and $Mg(OH)_2/MgO$ depicted in Figure 9a. The figure gives also charged states of Mg^{2+} and O vacancies, which create radiating impurity states in the gap at 3.1 -2.34 eV. Those are known to exist in Mg-based systems. The direct bandgaps of the two are shown at ~ 3.4 eV. A phase with low bandgap (3.43 eV) equal to that of Si (3.4 eV), with UV/blue photoluminescence was previously observed in incomplete conversion of $Mg(OH)_2$ to MgO. Also shown is the confinement gap of the silicon nanoparticle at ~ 2.1 eV. Because the shell is not spherical and most probably of a wide size distribution, we are unable to assign a confinement gap for the Mg-based system. The figure also shows photoexcitation at three wavelengths in the UV, blue and green at: 382, 487, and 546 nm respectively produced by an Hg mercury lamp. The spectral content of the light at the three wavelengths is given in Figure 9b. Figure 9c shows the bandgap diagram of amorphous MgO (a-MgO), crystalline MgO (c-MgO) and the $Mg(OH)_2/MgO$ phase.

The $Mg(OH)_2/MgO$ phase was related to charged states of Mg^{2+} and O vacancies, which create radiating impurity states in the gap at 3.1-2.34 eV. We also sketch in Figure 9a some known impurity states in the gap due to Mg^{2+} or O vacancies.[44–52] The band from which the emission emanates from the Si nanoparticles is over the range from 530-700 nm. Si nanoparticles or the Mg-based shell can absorb UV photons directly from the ground state into the conduction band states (above the band

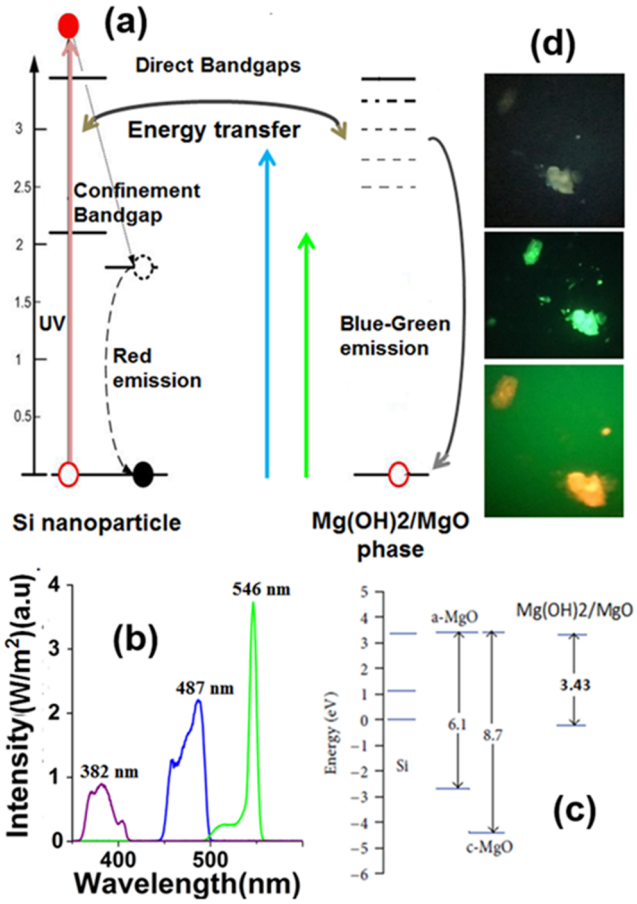

FIG. 9. (a) Partial energy band diagram of Si nanoparticles, and the $Mg(OH)_2$/MgO phase, showing direct bandgaps at ~ 3.4 eV for both. Also shown is the quantum mechanical confinement bandgap of the silicon nanoparticle at ~ 2.1 eV and the band from which the emission emanates from the Si nanoparticles. We also show some impurity states in the $Mg(OH)_2$/MgO gap due to Mg^{2+} or O vacancies. (b) Spectral distribution of the light used to excite sample using UV, blue and green light excitation. Those are shown as vertical arrows in (a). (c) The band energy diagram of a-silicon, c-silicon and $Mg(OH)_2$/MgO (d) wavelength-dependent imaging using a fluorescence microscopy, exciting a small area of the dried film, and showing images of clusters under UV, blue and green light at 382, 487 546 nm. Those are schematically labelled on the partial energy diagram in (a), and their spectral range are given in (b).

gap edge at 3.4 eV). This is followed by dephasing electronic relaxation into lower states in the gap of Si nanoparticles followed by radiative recombination to produce the red band. Absorption by the Mg-based shell of the UV photons may also directly take place from its ground state into conduction states above the band gap edge (3.4 eV). Photoexcited holes may relax to singly ionized oxygen vacancies in $Mg(OH)_2$ states just below the bandgap edge (near-band-edge (NBE) emission) where they radiatively recombination with an electron occupying the oxygen vacancies. Also, relaxation may proceed to the lower blue-green emitting states where recombination produces emission bands at 410, 432, 465, 495, and 534 nm (deep-level (DL) emissions). We note that the two systems are strongly coupled due to proximity made possible by the nanocomposite geometry. Moreover, because of near resonance of the edge state of the conduction bands, and some overlap of the emitting states of the two systems (see energy diagram), strong energy transfer can take place allowing strong absorption in Si to find its way to populate the strongly emitting states of the Mg-based shell enhancing the blue green emission.

Because hole attraction by the O-site is expected to be strong, photo excited holes diffuse to the side of Mg. The barrier to hole diffusion outside the silicon core limits such diffusion to the highest lying photo excited holes. Since the luminescence from the low-lying states is responsible for the red wing of the 500 to 800 nm luminescence band and falls well below the emitting states of the

Mg-system, the red wing of the emission band will be inhibited, resulting in a sizable blue-shift of the luminescence band. The large shift in the nanoparticle luminescence of 0.15 eV confirms the strong coupling and strong energy transfer processes between the shell and core electronically, effectively making them act as a single material of 3.4 eV bandgap. Moreover, the very small vibration signal of the free –OH group indicates that the present procedure converts $Mg(OH)_2$ to MgO without a high-temperature thermal treatment or calcination.

We conducted wavelength dependent imaging using a fluorescence microscope. We excited a small area of the dried film using excitation at 382, 487, 546 nm excitations shown in Figure 9d. Under UV radiation, the red and green-blue bands are expected to be emitted and the sample appears as white (Figure 9d top). The slight purple is due to direct scattering of the UV. Under 487 blue light only the MgO can be excited directly and the cluster may look green (Figure 9d middle). Under 546 nm green light only the nanoparticles are excited and the cluster appears red (Figure 9d bottom) gives the images of clusters.

Finally, since Mg(OH)2 and MgO can be converted into each other by either hydration procedures makes the hydroxide (Brucite) a flame-retardant filler in composite materials.[52] Future studies will focus on H_2 release due to reduction of Mg^{2+} in water by Si grains or Si-radical defects in silicates.

V. CONCLUSION

In conclusion, we integrated red-luminescent Si nanoparticles with Mg-based wide-bandgap insulators, forming strongly coupled, spatially inhomogeneous $Mg(OH)_2$/MgO–Si nanoparticle composite of "core-shell" geometry, nearly acting as a single material of a bandgap of 3.4 eV. The nanocomposite exhibit blue-green photoluminescence as well as red luminescence, covering most of the visible range 400-700 nm. Those features are consistent with strong energy transfer between the Si component and the Mg-based component due to formation of an intermediate $Mg(OH)_2$/MgO phase, with a direct bandgap of 3.43 eV that matches the silicon bandgap with enhanced formation of in-gap emitting states of charged Mg and O vacancies. With wide-bandgap and UV-visible luminescence, the nanocomposite architecture affords good luminescent material for photonic and PV applications.

[1] K. U. Kainer, *Magnesium Alloys and Technology* (DGM, 2006).
[2] J. E. Gray and B. Luan, J. Alloys Compd. **336**, 88 (2002).
[3] G. Song and D. StJohn, Corros. Sci. **46**, 1381 (2004).
[4] H. Tsuji, F. Yagi, H. Hattori, and H. Kita, J. Catal. **148**, 759 (1994).
[5] A. N. Copp, Am. Ceram. Soc. Bull. **74**, 135 (1995).
[6] A. Bhargava, J. A. Alarco, I. D. R. Mackinnon, D. Page, and A. Ilyushechkin, Mater. Lett. **34**, 133 (1998).
[7] Y. S. Yuan, M. S. Wong, and S. S. Wang, Mater. Res. Soc. **11**, 8 (1996).
[8] P. Yang and C. M. Lieber, Science **273**, 1836 (1996).
[9] B. M. Choudary, R. S. Mulukutla, and J. K. Kenneth (2003).
[10] M. Khalid, A. Setzer, M. Ziese, P. Esquinazi, D. Spemann, A. Pöppl, and E. Goering, Phys. Rev. B **81**, 214414 (2010).
[11] N. Kumar, D. Sanyal, and A. Sundaresan, Chem. Phys. Lett. **477**, 360 (2009).
[12] D. D. Wang, Z. Q. Chen, C. Y. Li, X. F. Li, C. Y. Cao, and Z. Tang, Phys. B Condens. Matter **407**, 2665 (2012).
[13] B. M. Maoz, E. Tirosh, M. Bar Sadan, and G. Markovich, Phys. Rev. B **83**, 161201 (2011).
[14] H. Wu, A. Stroppa, S. Sakong, S. Picozzi, M. Scheffler, and P. Kratzer, Phys. Rev. Lett. **105**, 267203 (2010).
[15] J. Alarcon, D. van der Voort, and G. Blasse, Mater. Res. Bull. **27**, 467 (1992).
[16] P. B. Devaraja, D. N. Avadhani, H. Nagabhushana, S. C. Prashantha, S. C. Sharma, B. M. Nagabhushana, H. P. Nagaswarupa, and B. D. Prasad, J. Radiat. Res. Appl. Sci. **8**, 362 (2015).
[17] A. Adamski, M. Wałęsa-Chorab, M. Kubicki, Z. Hnatejko, and V. Patroniak, Polyhedron **81**, 188 (2014).
[18] L. Kumari, W. Z. Li, C. H. Vannoy, R. M. Leblanc, and D. Z. Wang, Ceram. Int. **35**, 3355 (2009).
[19] G. Zou, W. Chen, R. Liu, and Z. Xu, Mater. Chem. Phys. **107**, 85 (2008).
[20] S. Utamapanya, K. J. Klabunde, and J. R. Schlup, Chem. Mater. **3**, 175 (1991).
[21] J. P. Hsu and A. Nacu, Colloids Surfaces A Physicochem. Eng. Asp. **262**, 220 (2005).
[22] H. Cao, H. Zheng, J. Yin, Y. Lu, S. Wu, X. Wu, and B. Li, J. Phys. Chem. C **114**, 17362 (2010).
[23] W. Fan, S. Sun, L. You, G. Cao, X. Song, W. Zhang, and H. Yu, J. Mater. Chem. **13**, 3062 (2003).
[24] H. Wu, M. Shao, J. Gu, and X. Wei, Mater. Lett. **58**, 2166 (2004).
[25] W. Feitknecht and H. Braun, Helv. Chim. Acta **50**, 2040 (1967).
[26] J. Green, J. Mater. Sci. **18**, 637 (1983).
[27] O. Akcakir, J. Therrien, G. Belomoin, N. Barry, J. D. Muller, E. Gratton, and M. Nayfeh, Appl. Phys. Lett. **76**, 1857 (2000).
[28] L. Mitas, J. Therrien, R. Twesten, G. Belomoin, and M. H. Nayfeh, Appl. Phys. Lett. **78**, 1918 (2001).
[29] G. Belomoin, J. Therrien, A. Smith, S. Rao, R. Twesten, S. Chaieb, M. H. Nayfeh, L. Wagner, and L. Mitas, Appl. Phys. Lett. **80**, 841 (2002).

[30] G. Belomoin, E. Rogozhina, J. Therrien, P. V. Braun, L. Abuhassan, M. H. Nayfeh, L. Wagner, and L. Mitas, Phys. Rev. B **65**, 193406 (2002).
[31] D. Nielsen, L. Abuhassan, M. Alchihabi, A. Al-Muhanna, J. Host, and M. H. Nayfeh, J. Appl. Phys. **101**, 114302 (2007).
[32] P. Casey and G. Hughes, J. Appl. Phys. **107**, 74107 (2010).
[33] S. G. Bratsch, J. Phys. Chem. Ref. Data **18**, 1 (1989).
[34] Y. Sakurai, T. Yabe, and K. Ikuta, Chinese Opt. Lett. **5**, 102 (2007).
[35] R. P. Donovan, *Contamination-Free Manufacturing for Semiconductors and Other Precision Products* (Dekker, 2001).
[36] G. Milazzo, *Electrochemistry: Theoretical Principles and Practical Applications* (Elsevier, New York, 1963).
[37] K. Shinoda, M. Yamakata, T. Nanba, H. Kimura, T. Moriwaki, Y. Kondo, T. Kawamoto, N. Niimi, N. Miyoshi, and N. Aikawa, Phys. Chem. Miner. **29**, 396 (2002).
[38] H. S. Jung, J.-K. Lee, J.-Y. Kim, and K. S. Hong, J. Colloid Interface Sci. **259**, 127 (2003).
[39] H. Dhaouadi and F. Touati, Nano-Micro Lett. **3**, 153 (2011).
[40] A. C. Chapman and L. E. Thirlwell, Spectrochim. Acta **20**, 937 (1964).
[41] I. Lutsyuk, Y. Vakhula, V. Levytskyi, and L. Zhuk, Chem. Chem. Technol. **8** (2014).
[42] L. Kumari, W. Z. Li, C. H. Vannoy, R. M. Leblanc, and D. Z. Wang, Ceram. Int. **35**, 3355 (2009).
[43] S. Balamurugan, L. Ashna, and P. Parthiban, J. Nanotechnol. **2014**, 1.
[44] H. Niu, Q. Yang, K. Tang, and Y. Xie, Microporous Mesoporous Mater. **96**, 428 (2006).
[45] H. Yufeng, G. Meng, Y. Changhui, Z. Xueru, and L. Zhang, J. Phys. Chem. B **109**(22), 11204–11208 (2005); Y. Hao, G. Meng, C. Ye, X. Zhang, and L. Zhang, *ibid.* **109**, 11204 (2005).
[46] G. H. Rosenblatt, M. W. Rowe, G. P. Williams, R. T. Williams, and Y. Chen, Phys. Rev. B **39**, 10309 (1989).
[47] G. P. Summers, T. M. Wilson, B. T. Jeffries, H. T. Tohver, Y. Chen, and M. M. Abraham, Phys. Rev. B **27**, 1283 (1983).
[48] N. C. S. Selvam, R. T. Kumar, L. J. Kennedy, and J. J. Vijaya, J. Alloys Compd. **509**, 9809 (2011).
[49] A. Kumar, S. Thota, S. Varma, and J. Kumar, J. Lumin. **131**, 640 (2011).
[50] D. G. Thomas, J. J. Hopfield, and W. M. Augustyniak, Phys. Rev. **140**, A202 (1965).
[51] Y. A. Valbis, K. A. Kalder, I. L. Kuusmann, C. B. Lushchik, A. A. Ratas, Z. A. Rachko, M. E. Springis, and V. M. Tift, JETP Lett. **22**, 36 (1975).
[52] R. N. Rothon, *Magnesium Hydroxide: New Products, Processes and Applications* (Intertech, Portland, MA, 2000).